CrossMark

Using VIRTIS on Venus Express to Constrain the Properties of the Giant Dark Cloud Observed in Images of Venus by IR2 on Akatsuki

Kevin McGouldrick[1] , Javier Peralta[2,3] , Joanna K. Barstow[4] , and Constantine C. C. Tsang[5]

[1] Laboratory for Atmospheric and Space Physics, University of Colorado Boulder, 3665 Discovery Dr., Boulder, CO 80303, USA
kevin.mcgouldrick@lasp.colorado.edu
[2] Facultad de Física, Universidad de Sevilla, Avd. de Reina Mercedes s/n, 41012 Sevilla, Spain
[3] Institute for Space and Astronautical Science, Japanese Aerospace Exploration Agency, 3-1-1 Yoshinodai, Chuo District, Sagamihara, Kanagawa, 252-5210, Japan
[4] School of Physical Sciences, The Open University, Milton Keynes, MK7 6AA, UK
[5] Department of Space Studies, Southwest Research Institute, 1050 Walnut St., Suite 300, Boulder, CO 80302, USA

Abstract

A cloud opacity contrast feature that has been called a "long-lived sharp disruption" has been seen in the atmosphere of Venus in the near-infrared using Akatsuki's IR2 camera, most clearly at equatorial latitudes. This feature was found to have a consistent planet-circling period of 4.9 days, and subsequent searches of past imagery revealed that it has probably existed for at least 30 years, the duration of near-infrared investigation of the deep atmosphere of Venus. Guided by the remarkably consistent morphological appearance of this feature, we have identified at least one previous instance of it in the Venus Express Visible and Infrared Thermal Imaging Spectrometer (VIRTIS) data. We take advantage of the spectroscopic capabilities of VIRTIS to retrieve atmospheric parameters in the vicinity of this feature that cannot be retrieved using the limited filter selection on board Akatsuki. We find that the changes in measurable quantities, such as cloud particle acid mass fraction, water vapor, carbon monoxide, cloud base altitude, and particle size, suggest that the changes that take place in the vicinity of this feature are restricted to the lower clouds of Venus (below 50 km). We hypothesize that further evolution of this feature (over timescales of days to weeks) results in measurable variations in these parameters at altitudes in the middle clouds of Venus (50–57 km), lending credence to its identification as a baroclinic trough or Kelvin front.

Unified Astronomy Thesaurus concepts: Venus (1763); Planetary atmospheres (1244); Atmospheric composition (2120); Atmospheric variability (2119); Atmospheric circulation (112); Near infrared astronomy (1093); Atmospheric clouds (2180)

Supporting material: data behind figure, interactive figure

1. Introduction

Peralta et al. (2020) have reported a persistent cloud feature that has been observed in data acquired by the Akatsuki spacecraft IR2 camera (Satoh et al. 2017). They noted that this feature was also evident in past observations of Venus in near-infrared emission, since shortly after the discovery of the technique by Allen & Crawford (1984), suggesting that this is a persistent feature of the present Venus climate. The IR2 nightside imagery revealed the existence of a large cloud feature spanning up to ±30° in latitude, maintaining its overall structure for days to weeks, and circling the planet Venus with an average period of about 4.9 days. A search of previously archived near-infrared night-side observations of Venus from a variety of platforms between 1983 (the discovery of the night-side imaging technique to assess the Venus cloud structure) and the present revealed evidence for the existence of this feature over nearly four decades. Here, we operate on the assumption that the feature seen in the Venus Express Visible and Infrared Thermal Imaging Spectrometer (VIRTIS) data— which predate the Akatsuki observations by nearly a decade— is functionally the same feature as reported by Peralta et al. (2020). In order to investigate changes to the cloud

characteristics associated with the passage of the front, we apply prior radiative transfer analyses (Barstow 2012; Barstow et al. 2012). First, we consider the immediate vicinity of the front by analyzing cubes in which a feature that morphologically resembles the front was identified. Next, we consider the medium-term evolution of the feature by analyzing two cubes obtained when the front was most likely on the opposite side of the planet from the observed field of view.

1.1. Complementary Noncontemporaneous Observations

The Akatsuki spacecraft orbits Venus at low inclination with a period of approximately 10 days, a periapse of a few thousand kilometers, and an apoapse of about 0.35 million km. Consequently, its imaging cameras are capable of acquiring global hemispheric views of the planet from a slowly varying vantage point for the majority of its operation. This enables the monitoring of atmospheric motions over nearly the entire viewable hemisphere for days at a time, the duration and cadence limited only by operational constraints of the instrument. The orbital motion of Venus means that there are effectively "observing seasons" during which the day side or the night side is preferentially viewed. Altogether, Akatsuki provides an excellent vantage point from which to characterize and assess the atmospheric dynamics of Venus.

However, Akatsuki's imagers carry only about a dozen filters among them, limiting the spectral scope of the mission

(Nakamura et al. 2007). Concurrent spectroscopy would potentially provide additional constraints on the atmospheric conditions and/or composition of the scenes viewed by the cameras, but Akatsuki does not carry any spectrometers, and no other active spacecraft currently orbits Venus. The Medium Resolution Infrared channel, VIRTIS-M-IR (Drossart et al. 2007), on Venus Express produced spectral cubes having a spectral range that contains the wavelength space observed by Akatsuki's IR2 camera. In this work, we utilize the combination of Akatsuki's capability of enabling analysis of atmospheric dynamics with Venus Express' capability of enabling spectrographic analyses of features in VIRTIS-M-IR data that bear strong morphological similarity to those seen in Akatsuki IR2 image data—namely, the sharp disruption (Peralta et al. 2020) and the "Giant Dark Cloud" (Satoh et al. 2019). Following the initial discovery of this feature in Akatsuki images, spectral observations of this feature were carried out using NASA's Infrared Telescope Facility (IRTF). That analysis is ongoing and will be the subject of a future publication.

1.2. Data

VIRTIS is a three-channel spectrometer (Drossart et al. 2007) that flew on board ESA's Venus Express spacecraft (Svedhem et al. 2009). Here, we make use of data from VIRTIS-M-IR. In a mapping mode of observation, this channel can obtain spectral cubes from about 1 μm to about 5 μm, with a nominal average spectral resolution $\lambda/\Delta\lambda \sim 300$. However, in practice, the spectral resolution was found to be about a factor of 2 more coarse (Bézard et al. 2009). The spatial resolution of VIRTIS-M-IR is 250 μrad, which at a typical apoapse distance from Venus of 66,000 km equates to about 16 km pixel^{-1}.

In this paper, we analyze only a handful of VIRTIS cubes. A feature resembling that reported by Peralta et al. (2020) was identified in spectral cubes obtained during orbit 517. We explore the immediate response of the atmosphere and clouds to the passage of this feature by analyzing these cubes. In addition, we consider that longer-term evolution of the feature can be assessed by analyzing cubes that fall somewhere in the wake of the predicted location of the feature. A previous analysis of VIRTIS cubes 383 and 384 exists in the literature (McGouldrick et al. 2012), so we chose those orbits to extend our compositional analyses.

One aspect of the work presented here is the analysis of the temporal evolution of the features seen in the Akatsuki data as reported by Peralta et al. (2020) and Satoh et al. (2019). VIRTIS, on board the highly inclined Venus Express spacecraft often viewed equatorial latitudes only near the limb where features would have been significantly foreshortened. Furthermore, the field of view of VIRTIS-M-IR was only about 10% of the full disk at apoapse, and spacecraft operations limited the use of the VIRTIS instrument to a maximum of only about 6 hr per orbit. As a consequence, the likelihood of capturing this feature at any given time was low, and the likelihood of certain identification of it even when it was seen lower still. However, the analysis by Peralta et al. (2020) indicated that the feature persisted throughout the functional lifetime of Akatsuki's IR2 instrument and suggested that it persisted—or at least recurred—throughout nearly four decades of observation of the Venus night side in the near-infrared. Furthermore, the analysis of the feature by Peralta et al. (2020) suggests that the structure of the

clouds evolves with distance (i.e., time) in the wake of the feature. Based on this evidence, we assume for the purposes of this work that the feature is persistent, and existed throughout the Venus Express mission. We further assume that the distance of the clouds behind the feature—that is, after the feature has passed—can provide information regarding the time evolution of the clouds in response to the perturbation caused by the passage of the feature. That is, once we identify the occurrence of the feature in VIRTIS data at a given time and place (longitude), we can estimate the longitude of the feature at any past or future time and place the clouds in a time frame relative to the time of the feature passage.

2. Methods

Our spectrographic analysis is adapted from the previous work by Barstow et al. (2012) and updated by Barstow (2012). That work was a multispectral application of NEMESIS (Irwin et al. 2008), using the "band ratio" technique. Following Barstow et al. (2012), we generate retrieved H_2O and CO mixing ratios, acid mass fraction of the cloud droplets, altitude of the cloud base, and particle size parameter (an estimate of the relative abundance of mode 2-sized and mode 3-sized droplets) for all of the high spatial (256×256 pixels) and spectral (432 channels covering the range 1–5 μm) resolution night-side mapping mode cubes obtained with substantial night-side coverage. We utilize the "CALIBRATED" data set and the "GEOMETRY" data cubes for this analysis. Data sets of the VIRTIS instrument were downloaded from the ESA Planetary Science Archive[6] (Besse et al. 2018).

The calibrated data were corrected for stray solar light, largely following the procedure outlined in Barstow et al. (2012) and Barstow (2012). A sample scattered solar spectrum was obtained from an image of empty space, scaled to each image according to the radiance at 1.41 μm (where the contribution from Venus emission should be nil, due to strong absorption by CO_2). We then removed background thermal radiance that results from changes in the detector temperature by fitting an exponential function of wavelength to the radiance—averaged over the slit dimension—detected at the places of greatest atmospheric absorption due primarily to CO_2 and H_2O, but in some cases also other species such as OCS, SO_2, CO, and HCl— $(1.06 \pm 0.01)\,\mu$m, $(1.225 \pm 0.015)\,\mu$m, $(1.08 \pm 0.03)\,\mu$m, and $(1.57 \pm 0.03)\,\mu$m—where the expected emitted radiance should be zero. The estimated thermal spectrum so acquired is applied to the full VIRTIS-M-IR spectral cube—extrapolating beyond the longest wavelength used in the fit (1.60 μm).

The resulting cubes are then masked, restricting analysis only to pixels where the emission angle is less than 85°, solar incidence angle is greater than 95°, and local solar time is between 18^h20^m and 5^h40^m. A limb-darkening correction, following Carlson et al. (1993) and Barstow (2012), is then applied such that $I_0 = I_{\text{measured}}/(0.3211 + 0.684\,8\cos\epsilon)$, where ϵ is the emission angle. This limb-darkening correction so derived is dependent upon the vertical structure of the cloud model assumed by those authors; differences in the vertical structure of the clouds can affect the validity of this correction factor, especially at higher emission angles. Unlike Barstow (2012), we apply this correction factor to all wavelengths equally. Our reasoning for this is that the differences between the wavelength-dependent correction factors previously

---

6 http://archives.esac.esa.int/psa

calculated by Barstow (2012) were so subtle that uncertainties in the vertical structure of the cloud and even the measured radiance were larger in magnitude. Finally, all pixels exhibiting a limb-darkening corrected 1.74 μm radiance of less than 0.05 W m^{-2} sr^{-1} μm^{-1} are masked out because the diminishing signal results in too poor a signal-to-noise ratio (S/N) in such low radiance conditions.

Each wavelength slice of the cube is then convolved with a Gaussian point-spread function having a radius of 10 pixels and FWHM of $2\sqrt{10} \approx 6.3$ pixels, using a reflection boundary condition for calculations within 10 pixels of the image edges (using the IDL astronomy library `filter_image` procedure). This filtering is comparable to stacking $\pi \cdot \text{FWHM}^2 = 40\pi \approx$ 125 spectra for each reported pixel. This is about one-third the number of stacked spectra than the 20×20 binning that Barstow et al. (2012) and Barstow (2012) applied, but we found that the chosen parameters adequately improved the S/N, enabling this analysis. The consequence of this smoothing is a reduction of the nominal spatial resolution of the VIRTIS slices from about 250 μrad to about 1600 μrad. At nadir, from the apoapse distance of 6.6×10^4 km, this results in a smoothed spatial resolution of about 100 km, though at closer distances, the spatial resolution will of course improve. In addition, the S/N is improved by a factor of about $\sqrt{40\pi} \approx 11$. Note that because we apply this filtering to all pixels, the information in the gradient is not lost. Using the noise equivalent spectral radiance (NESR) as a baseline, we can estimate the S/N for the observational data presented here. Moinelo et al. (2010) and Piccioni et al. (2008) have measured the NESR for VIRTIS. The common log of the NESR for VIRTIS-M-IR can be approximated as a quadratic for the wave bands considered here. Hence, we approximate the dependence of NESR on wavelength (λ) and exposure time (t_{exp}) as follows:

$$\text{NESR} = \sqrt{t_{\text{exp}}^{-1}} \cdot 10^{0.2375\lambda^2 - 1.5724\lambda - 1.0798}. \qquad (1)$$

For the particular cubes investigated here (`517_01`, `517_03`, `383_00`, and `384_00`), $t_{\text{exp}} = 3.3$ s, so that within the spectral range considered here, the NESR ranges from a maximum of about 4.4×10^{-4} W m^{-2} sr^{-1} μm^{-1} at 1.74 μm to a minimum of about 1.6×10^{-4} W m^{-2} sr^{-1} μm^{-1} at 2.53 μm. For the median radiance at each of these wavelengths, this translates to an S/N of about 400 at 1.74 μm to about 10 at 2.53 μm. These S/Ns are improved to about 7000 and 150 upon application of the spectral stacking.

We then extract the data from the cubes in order to calculate the retrieval parameters according to the polynomials provided in Barstow (2012). Because the spectral registration varies in response to the detector temperatures, the target wavelengths do not always neatly match the spectels (pixels in the spectral dimension) of the detector. In order to account for this, we define the radiance at each target wavelength (except for the 2.53 μm radiance) to be the radiance interpolated between the bracketing spectels and weighted according to wavelength. However, because the radiance at 2.53 μm is particularly low, it is exceptionally susceptible to uncertainties that result from the even/odd effect that exists even in calibrated VIRTIS-M-IR data (Moinelo et al. 2010). At this wavelength, following Barstow et al. (2012) and Barstow (2012), we apply a second-degree binomial filter, centered on the wavelength that is closest to the target value of 2.53 μm.

Barstow (2012) developed polynomials to approximate the retrievals of various constituents of the Venus atmosphere through a series of retrievals and corrections. First, the mass fraction of acid and the carbon monoxide mixing ratio were retrieved, using radiance at 1.74, 2.2, 2.29, and 2.32 μm. Next, the radiance in the remaining spectral bands at 2.41 and 2.53 μm were corrected for contributions from the mass fraction of acid and the CO mixing ratio, before they are utilized to retrieve the water vapor mixing ratio below the clouds and the cloud base altitude. The details of this process can be found in Barstow (2012). We then extract the Carlson et al. (1993) size parameter (unitless). We utilize the size parameter introduced by Carlson et al. (1993) and by Wilson et al. (2008) in order to assess the typical particle sizes because we were not able to reproduce the Barstow (2012) M3:M2 (mode 3 to mode 2) ratio of droplet size modes, possibly due to changes in the calibration procedures. Ultimately, because the cloud particle size distributions are not as homogeneous as assumed by the prior NEMESIS modeling—even though the size parameter leaves ambiguous the relative contribution of number and size of particles to measured differences—reverting to this parameter for insight likely permits a more realistic analysis than the ratio of total numbers of mode 2 and mode 3 particles returned by the previous efforts.

To explore the characteristics of the Giant Dark Cloud, we further apply a combined geometry and data mask, limiting the valid points to those having latitude north of 30°S . The latitude restriction is applied because the Giant Dark Cloud is reported to occur only equatorward of 30° in Akatsuki observations Next, binning the data in intervals of 1° in latitude, we determine the longitudinal position of the feature boundary by finding the minimum gradient of the 1.74 μm radiance and shift the data at that latitude to match the longitude of the feature at 30°S latitude. We repeat this procedure, moving from south to north at all latitude bands between 30°S and 10°S. Finally, we overplot the mean value as a function of longitude for each shifted and stacked data set.

3. Results

Because we have made some adjustments (and hopefully even improvements) to the reduction of the data with regard to the correction of scattered sunlight effects, we do not present this comparison on a per-spectrum basis, but rather summaries of the mean and standard deviation on a per-orbit basis. In all cases, the trends are both qualitatively and quantitatively similar to the corresponding plots in Figure 5.1 of Barstow (2012). The most significant difference is the carbon monoxide exhibiting greater frequency of larger measured values ([CO] > 50 ppmv) at lower radiances. This is likely due to the increase in uncertainty that results from the analysis of points with 1.74 μm radiances smaller than 0.05 W m^{-2} sr^{-1} μm^{-1}.

First we demonstrate in Figure 1 that we have qualitatively reproduced the full-data set analyses by Barstow (2012), which increases confidence in our more localized analysis to follow. The retrieved acid mass fraction is between 85% and 90% at low radiance, and decreases to 70% at higher radiance in Barstow (2012), while ours is 85% at low radiance, and decreases to about 60% at high radiance. The cloud base altitude is at a minimum of about 47.5 km at both low and high radiances, and reaches a peak of just under 50 km at about 0.15 W m^{-2} sr^{-1} μm^{-1} in both analyses. The particle size estimator—whether size parameter or M3:M2 ratio—tends
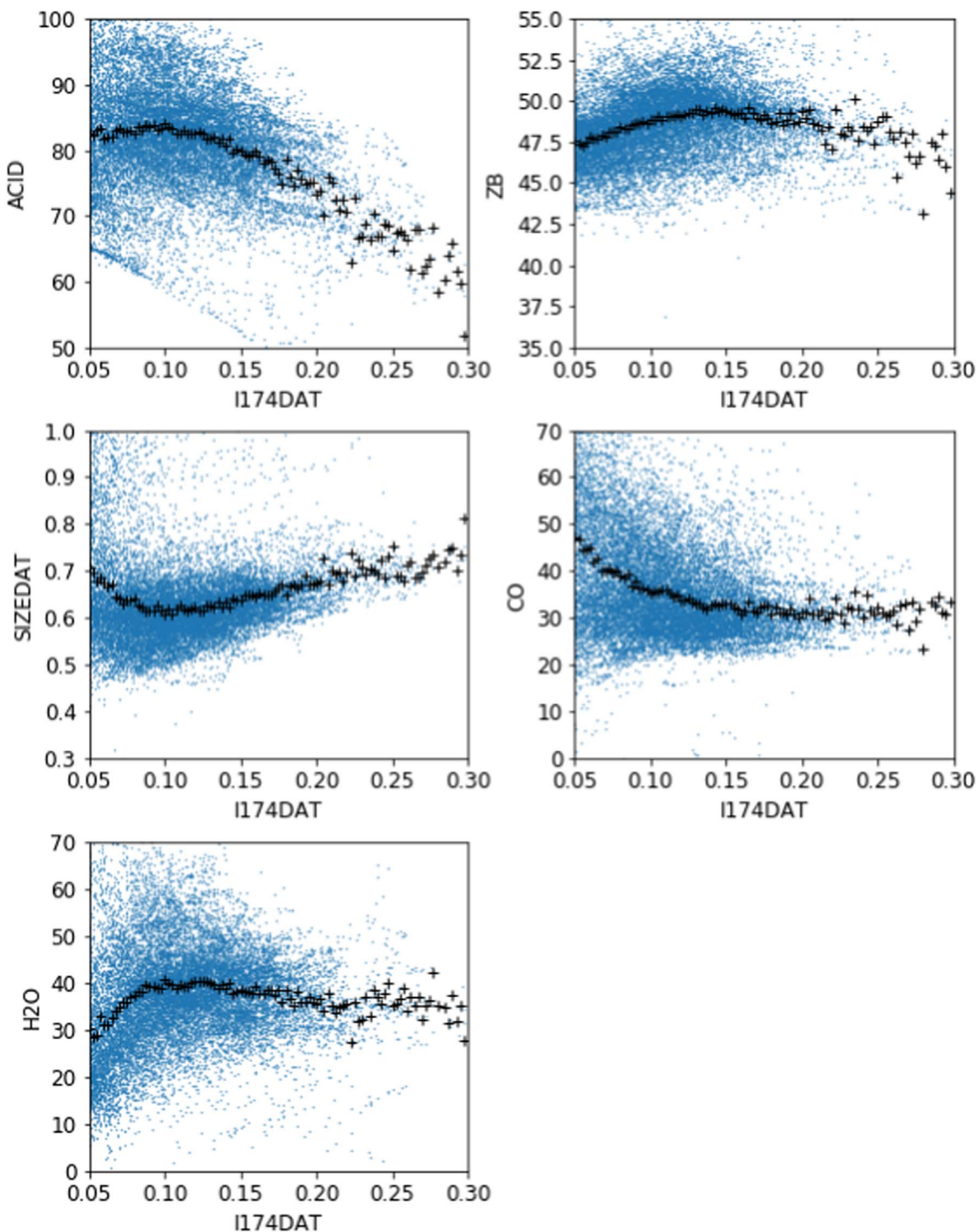
Figure 1. Scatter plots of (UL) acid mass fraction, (UR) cloud base altitude, (MR) size parameter, (ML) carbon monoxide, and (LL) water vapor above 30 km, as functions of 1.74 μm radiance. Each point represents the median value of non-masked data acquired in mapping mode during a single orbit. The crosses (+) indicate the mean of the retrieved values binned to 0.0025 W m^{-2} sr^{-1} μm^{-1} in radiance (see Figure 15 of Barstow et al. 2012). A similar comparison, but using median values rather than averages is included as an extended version of this figure.

(The data used to create this figure are available.)

from a balance toward small particles at low radiance and large particles as high radiance in both analysis; however, ours indicates an increase of large particles at the lowest radiances, in contrast with Barstow (2012). The CO in both analyses is relatively constant near 30 ppmv, with a discrepancy in which Barstow (2012) indicated a slight decrease at low radiance, while we see a notable increase. The water vapor mixing ratio in both analyses shows a peak approaching 40 ppmv around 0.10 W m^{-2} sr^{-1} μm^{-1} with a more significant decrease toward low radiance than toward high radiance. Quantitatively, our measurements of water vapor mixing ratio typically are slightly greater than those of Barstow (2012) by about 5 ppmv.
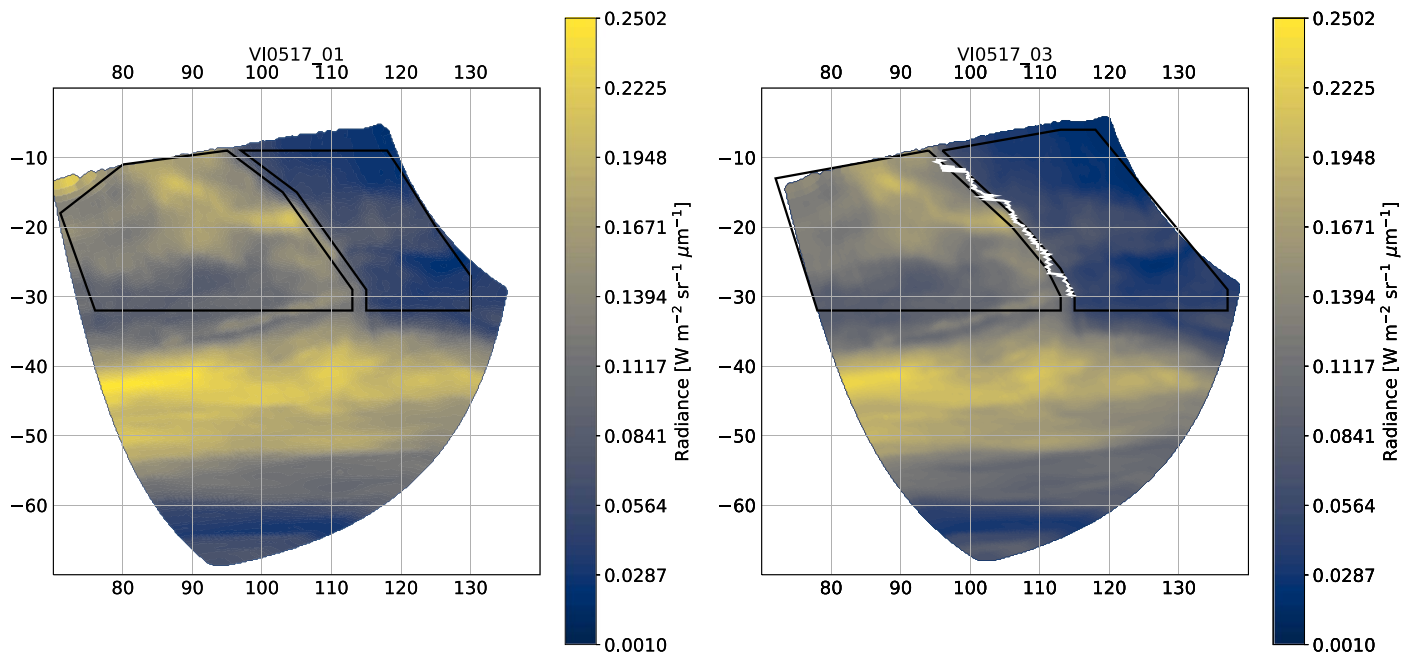
Figure 2. 1.74 μm radiance from image cubes `VI0517_01` and `VI0517_03`, plotted on a longitude/latitude Cartesian grid defined by the `VI0517_01` observation. The `VI517_03` data have been shifted to the east by 3°061 longitude, to demonstrate the 4°9 day^{-1} speed of this feature. A grid has been added to each map to facilitate comparison between the two frames. The regions of interest discussed in Section 4 and summarized in Table 1 are identified as closed irregular polygons; "ahead" is to the west (left) of the boundary and "behind" is to the east (right) of it. The algorithm-calculated location of the front—the maximum negative gradient in 1.74 μm radiance between the 10° and 30° south latitudes—is indicated as a locus of points in white, between the ahead and behind ROIs.

As mentioned in Section 1, Peralta et al. (2020) pointed out that features having morphological and dynamical similarity to the sharp disruption seen in the Akatsuki IR2 data were found in the VIRTIS-M-IR cubes. In Figure 2 we show two slices of 1.74 μm radiance taken during orbit 517, separated by 54 minutes. The second slice, `VI0517_03`, is shifted eastward in longitude to compensate for the observed 4.9 days planet-circling speed of the feature reported by Peralta et al. (2020). This simple shift in longitude assumes solid-body rotation over all affected latitudes. Figure 3 includes a looping two-frame animation of these two longitude-adjusted frames (without the ROI information).

In order to understand the nature of the changes that occur as a result of the passage of this feature, we apply the retrievals from Barstow et al. (2012) and Barstow (2012) to the individual cubes. Though we have performed the analysis on both cubes, because there were no evident differences between them, we show only `VI0517_03`. Example VIRTIS-M-IR spectra (before the stacking described in Section 2) from the regions ahead of and behind the propagating disruption as seen during Venus Express Orbit 517 are shown in Figure 4. In Figure 5, we present a stacked transect for each of the retrieved parameters as a function of longitude. To produce these plots, we carry out the procedure described in Section 2.

The acid mass fraction in Figure 5, though exhibiting ±5% variability, is fairly constant at about 81% west of (i.e., ahead of) the boundary, but rises sharply to 87% before relaxing back to about 85% east of (i.e., behind) the boundary.

The CO mixing ratio shows no significant variation at the boundary, though there is a 7 ppmv increase in retrieved mixing ratio about 10° longitude behind it. While the General Circulation Model simulations shown in Peralta et al. (2020) indicate that the proposed Kelvin wave would have a vertical structure leading to a "phase lag" in response at lower altitudes, compared with the cloud altitudes, the angle of this vertical
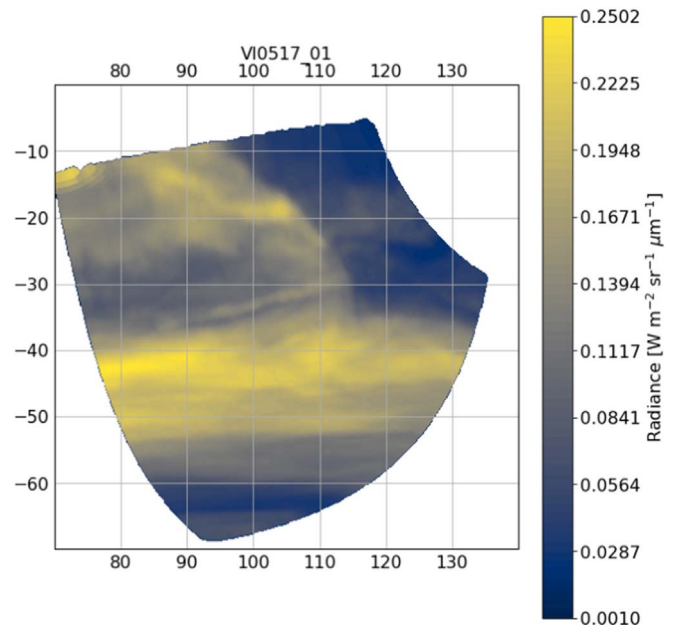
Figure 3. A two-frame "blink" movie driven by a java applet is provided as an interactive figure available in the online publication. This interactive figure demonstrates the relative motion of the cloud structure relative to the boundary (which is held "in place" by applying a 4°9 day^{-1} advection to the later image).

structure is too steep in the simulated atmosphere to be responsible for the behavior seen in the observational data. Specifically, the wave seen in the GCM lags at a rate of approximately 10° km^{-1}, which would lead to a ~150° longitude lag, much larger than the 10° seen. Such a rapid change in the carbon monoxide mixing ratio would be very unexpected, as there are no known drivers that could cause it. Specifically, the chemical timescales involved are very long
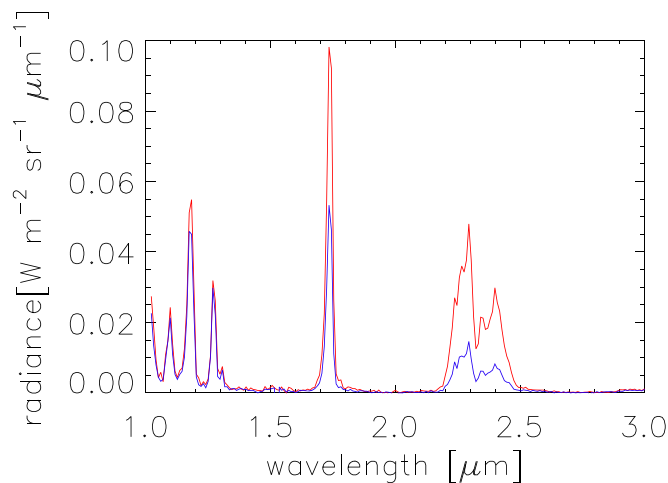
Figure 4. Selected spectra extracted from the `VI0517_01` data cube of points in the "ahead" ROI (red) and "behind" ROI (blue), demonstrating the spectral differences in these two regions.

compared with the passage of such a front (Yung et al. 2009). This is in contrast with the rapid timescale for the microphysics variations that we claim to see in the variation of the water vapor mixing ratio, droplet acid mass fraction, and droplet size parameter. The growth timescales in the lower and middle cloud decks of Venus are much faster than the transport timescales (James et al. 1997; McGouldrick & Toon 2007), and the hydroscopic nature of the sulfuric acid cloud droplets makes the equilibration process faster still (Steele & Hamill 1981). On the other hand, as seen in the 1.74 μm radiance transect, the cloud opacity is very high in this region, and many points are masked out due to low radiance. Possibly, this slight increase is simply the result of poor S/N.

The cloud base altitude (z_{base}) drops by nearly 2 km west to east across the boundary, from about 49.3 km down to about 47.5 km. Also noteworthy is the steady increase in the cloud base altitude for about 20° longitude ahead of the boundary, increasing from about 48.2 km.

The water vapor mixing ratio is fairly constant at about 40 ppmv ahead of the boundary before dropping sharply to just under 30 ppmv behind the boundary. The water vapor also exhibits a slight increase of a few ppmv in the immediate vicinity of the boundary before this decay. Also notable is that the drop in water vapor mixing ratio occurs exclusively behind the boundary, while all of the other measured properties exhibit the beginning of their trends a few degrees longitude before the boundary.

Finally, the size parameter also is seen to be fairly steady at 0.625 ahead of the boundary, with perhaps a slight negative gradient from west to east. However, it drops sharply to 0.575 across the boundary, before beginning to increase again less than 10° longitude behind the boundary.

The water vapor mixing ratio in the lower opacity region ahead of the transition is somewhat larger than the previously measured subcloud water vapor mixing ratios, which have tended to be around 30 ppmv (Pollack et al. 1993; Marcq et al. 2008; Bézard et al. 2009; Arney et al. 2014). However, some previous observations and models do in fact reach values this high, so they are perhaps not unreasonable (Ignatiev et al. 1997; Gao et al. 2014). The 20 ppmv that was retrieved in the darker regions behind the transition is somewhat low for the nominal retrieval altitude, the weighting function of which

peaks at about 35 km. However, it is consistent with previously observed water vapor mixing ratios at the higher altitudes of the cloud tops, both in models and in observations (James et al. 1997; Fedorova et al. 2016; McGouldrick 2017). It is also about a factor of 2 larger than the cloud top water vapor measured by Fedorova et al. (2016). Note, however, that the radiance at 2.41 μm, from which the water vapor retrieval is calculated, also exhibits significant sensitivity to the total cloud opacity. Hence, in the case where increased cloud opacity exists, the contribution to the radiance by water vapor will occur correspondingly higher in the atmosphere. Because a significant vertical gradient in the water vapor concentration is known to exist from both models (James et al. 1997) and observations (e.g., Bézard et al. 2009; Cottini et al. 2015), it can be expected that increased cloud opacity would tend to result in lower water vapor retrievals.

4. Discussion

One thing is certain from these measurements: the boundary represents a clear change in the nature and/or structure of the atmosphere and clouds. Because the radiative transfer models used by Barstow et al. (2012) and Barstow (2012) were not responsive to significant variations in the cloud particle size distributions—the numbers of the set modes of particles were varied, but the size distributions themselves are not—a distinct possibility is that the cloud particle size and vertical distributions differ sufficiently from the model standards so that the retrievals obtained behind the boundary are simply unreliable. Correcting this would require rewriting the NEM-ESIS radiative transfer retrieval analyses and rederiving the retrieval polynomials to respond to a wider range of cloud particle size free parameters. Such work, though already underway by the co-authors, is beyond the scope of this paper.

A second caveat is that the retrievals exhibit very low S/N when the 1.74 μm radiance falls below 0.05 W m^{-2} sr^{-1} μm^{-1} (Barstow 2012; Barstow et al. 2012). In such high cloud opacity regions, the emitted radiance at key wavelengths in the 2.2–2.6 μm spectral window complex will drop below the NESR. Hence the retrievals in such regions are highly uncertain due to low S/N. The dark cloud observed behind the boundary in these images is very dark indeed, and a significant fraction of points falls below this critical threshold, especially at "shifted" longitudes eastward (rightward) of 120° (see Figure 5(a)). Consequently, the data in Figure 5 that lies in that region must also be taken with a grain of salt.

These caveats having been presented, what story do the data tell? The sharp decline in 1.74 μm radiance already indicates a significant increase in cloud opacity. Other than scattering by cloud particles, the only other sources of extinction near this spectral window are gaseous water vapor and gaseous hydrochloric acid (HCl). However, the abundance of HCl is too low to produce such a substantial change, and the water vapor retrieval suggests instead a decrease in abundance, and so cannot be directly responsible for the increase in opacity at this wavelength. But what drives the change in cloud opacity? Or, alternately, what does this change in cloud opacity do to the Venus atmosphere? The cloud base altitude decreases by nearly 2 km as the cloud opacity increases, suggesting that this increase in cloud opacity is likely to be occurring in the lower clouds. This would be consistent with previous observations of the variations in the Venus clouds. The Pioneer Venus Large Probe Cloud Particle Size Spectrometer (LCPS) data suggests
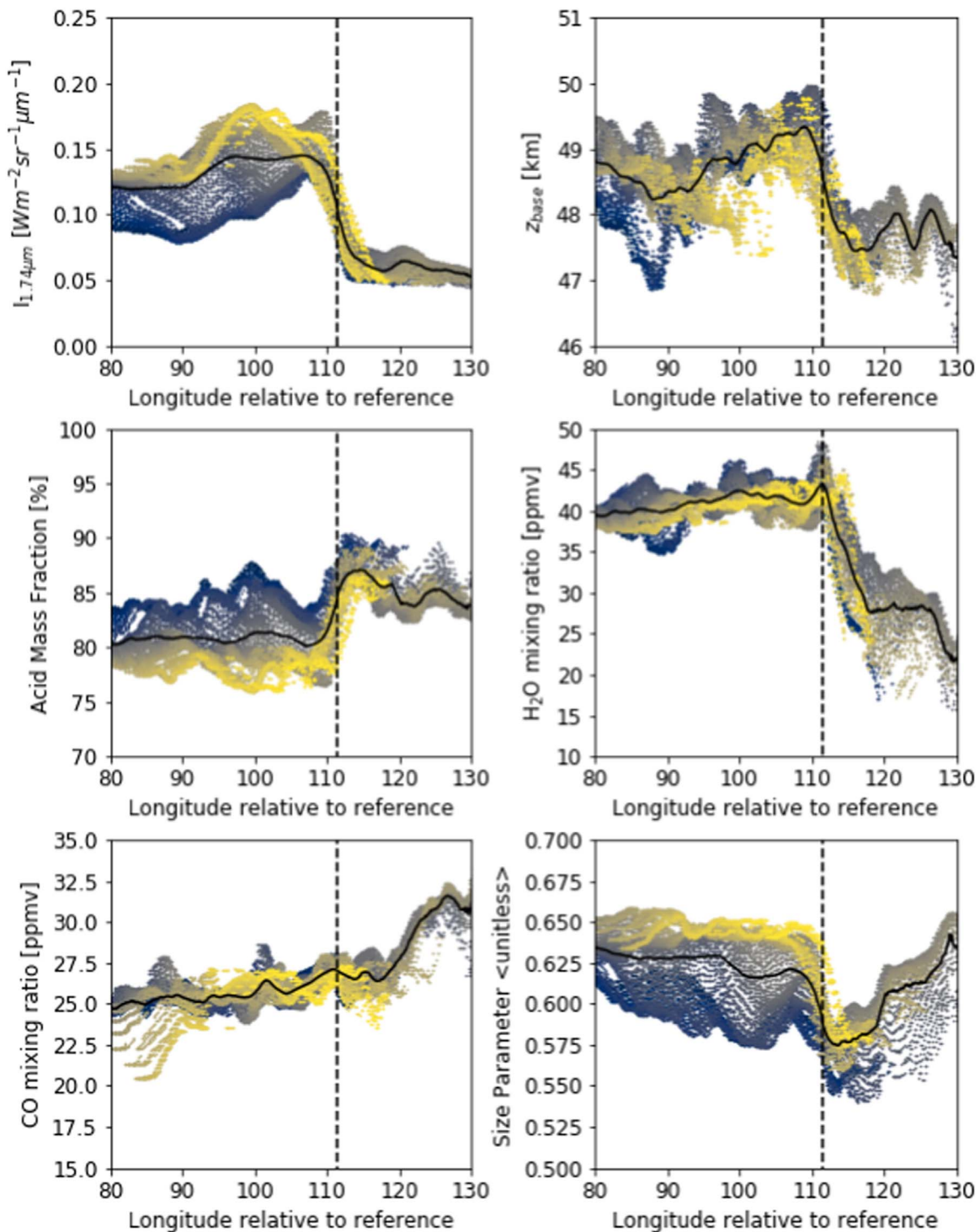
Figure 5. Zonal transects across the feature boundary for each of the retrieved parameters discussed in this paper: (UL) radiance, (UR) cloud base altitude, (ML) acid mass fraction, (MR) H_2O mixing ratio, (LL) CO mixing ratio, and (LR) size parameter. Each point represents a retrieval from a point in the remapped image, while the black line represents the binned mean retrieved value as a function of (shifted) longitude. The boundary is defined to be the location of the steepest zonal gradient in 1.74 μm radiance at each sampled latitude, and the successive transects are all shifted so that this boundary is plotted here at the longitude where it is found at 30°S latitude (denoted by the vertical dashed line in each subplot). Note that all parameters except for CO mixing ratio exhibit a significant gradient at or near this boundary. The color of the plotted symbol denotes latitude, ranging from blue at 30°S to yellow at 10°S; the color scheme is the same as used in our images (Figures 2 and 6).

that the lower cloud between 48 and 50 km is responsible for fully half of the cloud opacity (Knollenberg & Hunten 1980; Pollack et al. 1980). And, previous analysis of Galileo NIMS observations of Venus indicated that the observed opacity variations were dominated by changes in the lower clouds at altitudes of 48–50 km (Grinspoon et al. 1993). However, the

speed of the feature is more consistent with the mean zonal winds at the altitude of the upper clouds (at 57 km), suggesting that this phenomenon could be driven by processes occurring in the upper clouds.

We suggest that the passage of a wave having a phase speed greater than that of the mean zonal winds at the altitude of the

condensational cloud decks of Venus (50–57 km) triggers a response in the clouds themselves that draws the influence to depth. The above observations are consistent with the identification of this phenomenon as a front associated with a supercritical nonlinear Kelvin wave (Fedorov & Melville 2000), as suggested by Peralta et al. (2020). A Kelvin wave is nondispersive, indicating that it propagates with the same phase speed, regardless of frequency (or altitude in the atmosphere). Any propagating internal buoyancy wave (such as an equatorially trapped Kelvin wave) requires a perturbation that displaces the fluid from equilibrium in order to generate the wave. On Earth, a common source of equatorially trapped Kelvin waves is the incidence of enhanced convection over the Pacific Ocean associated with the Madden-Julian Oscillation and the El Niño Southern Oscillation (Emanuel 1987). The Y-feature (or ψ-feature) that has been observed with a 4 day period in the Venusian cloud tops is another example. While the mechanism for the excitation of a Venusian Kelvin wave with a 4.9 day period is yet to be elucidated, a potential driver could be thermal tides driven by absorption of incident solar radiation by SO_2 and the unknown absorber in the upper Venus atmosphere. The observed phase speed of $91\,\mathrm{m\,s^{-1}}$ is consistent with a roughly 1 km thick thermocline, lending credence to this suggestion because such a narrow thermocline is more consistent with the effects of solar heating in the strongly stable upper clouds than that set up by radiative cooling to space in the middle and lower clouds.

However, at deeper altitudes, where the zonal winds are slower and the atmospheric density is greater, the advancing Kelvin wave produces a local air density maximum in the form of a hydraulic jump at the leading edge of the wave front. This density maximum triggers narrow downwelling plumes similar to those seen in numerical compressible convection simulations by Baker et al. (1998). These narrow downdrafts—smaller scale than the observed spatial resolution—lead to the marginal clearing and slight increase in retrieved water vapor mixing ratio immediately ahead of the front. These downwellings rapidly reach the subcloud altitudes, where increased air density halts their descent and results in the formation of broad regions of somewhat weaker upwelling (Baker et al. 1998). As shown by the microphysics simulations of McGouldrick & Toon (2008), this upwelling will initially result in both a deepening of the cloud base altitude by about 2 km and a decrease in the typical particle size as new activation of particles produces a population of small droplets that dominates the larger droplet population (see Figures 6, 8, and 10 of that paper). Because the newly formed cloud is dominated by particles in the lower cloud region, where higher temperatures result in larger equilibrium acid mass fraction, this new cloud formation drives an increase in the retrieved acid mass fraction. This condensation will also reduce the available water vapor, as it is taken up into cloud particles at a rate defined by the equilibrium mass fraction; but this change is too small to explain the 15 ppmv decrease observed in the retrieved water vapor mixing ratio. There are two possible reasons for this. Either the retrieved water vapor in the darker cloud region —for reasons discussed earlier in Section 3—is inaccurate, or the rapidly thickening cloud shifts the peak of the water vapor mixing ratio weighting function to higher altitudes (see Figure 4.7 of Barstow 2012). Hence, once the thick cloud forms, the water vapor retrieval samples a higher altitude, where previous models (Imamura & Hashimoto 1998) and observations

(Cottini et al. 2015; Fedorova et al. 2016) demonstrate the water vapor mixing ratio to be lower.

The increase in the acid mass fraction is a little more puzzling in the above hypothesis. If, like the water vapor retrieval, this measurement is more sensitive to the cloud tops because of the increased cloud opacity, then we might expect the acid mass fraction to exhibit a smaller value, more consistent with that seen at the cloud tops. On the other hand, if the decrease in 50 km water vapor is real and not an artifact of changes to the weighting function, then the lower water vapor mixing ratio ought to drive an increase in the acid mass fraction, just as we see here. Finally, because the bulk of the increase in cloud mass occurs in the deeper parts of the cloud, it is likely that this localized change affects the overall retrieved acid mass fraction. Because the equilibrium acid mass fraction is typically greater at these deeper altitudes, and because the polynomials of Barstow (2012) assume a constant acid mass fraction throughout the clouds, an increase in the cloud mass that is localized to the lower clouds will tend to result in a larger average cloud acid mass fraction when averaged over the entire cloud column. Theoretical calculations based on the parameterization by Steele & Hamill (1981) suggest that the equilibrium acid mass fraction ought to change only by a few percent near the cloud base, if the water vapor mixing ratio there were to decrease to 25 ppmv. Because the retrieval algorithms defined by Barstow et al. (2012) assume constant acid mass fraction throughout the clouds, we believe this latter explanation to be more credible. The previous two paragraphs demonstrate that the retrievals of the acid mass fraction and the water vapor mixing ratio are not completely consistent with each other. Based on previous work by Barstow et al. (2012), and the above discussion, we consider the retrieval of the acid mass fraction to be somewhat more robust. However, the assumption of a constant vertical profile of the acid mass fraction limits the likelihood of the veracity of the retrieved value for all altitudes within the middle and lower clouds. Similarly, previous work by Tsang et al. (2008) demonstrates the high uncertainty in the retrieval of H_2O mixing ratios from the 2.41 μm water vapor absorption feature in the Venusian near-infrared spectrum. Note also that Barstow et al. (2012) report a ± 10 ppmv uncertainty in the water vapor mixing ratio retrieval. A pessimistic interpretation of that uncertainty applied to the present work would render all conclusions regarding water vapor to be null. At the very least we can say that improved spectral analysis of the variability of subcloud water vapor would be necessary to thoroughly quantify the hypothesis presented here, as far as the implications for water vapor are concerned.

Eventually, well behind the passing wave, the broad and weak upwelling will have lost its impetus, allowing the cloud to continue to evolve in the absence of such dynamical forcing. Specifically, the droplets would gradually become more well mixed throughout the cloud, rather than remaining concentrated largely in the lower cloud region below 50 km, as they do in the immediate aftermath of the wave. The particles also would gradually grow larger by both condensation and coagulation, resulting in an increase in the size parameter. At the same time, as the cloud mass becomes more evenly distributed throughout the cloud, the contribution to the acid mass fraction retrieval will also become more evenly distributed with altitude, resulting in a decrease in the retrieved acid mass fraction. Due to this transition to overall larger and
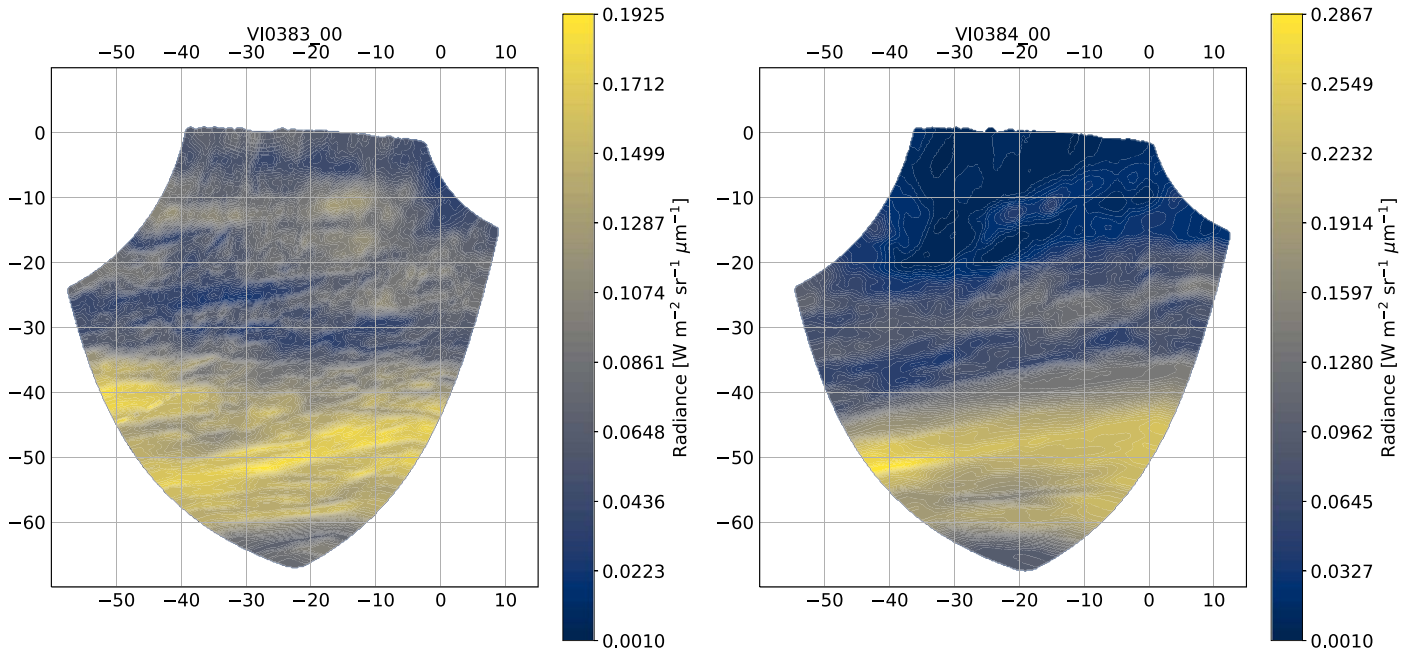
Figure 6. 1.74 μm radiance from image cubes `VI0383_00` and `VI0384_00`, plotted on longitude/latitude Cartesian grids. We hypothesize that the northern dark region in each cube is an evolved form of the dark cloud shown being formed in the `VI0517` cubes (Figure 2).

fewer cloud droplets (and reduction in cloud mass), the total cloud opacity decreases, causing the contribution of the cloud region to the water vapor retrieval to become less significant, resulting in a higher retrieved water vapor mixing ratio in brighter regions.

As discussed previously in Section 1, we are operating under the assumption that this Kelvin front is a persistent feature in the Venus atmosphere, constantly circling the planet at equatorial latitudes, and at a typical planet-circling period of 4.9 days. As such, having identified the position of this feature during orbit 517, we can determine its approximate location at any other time. At a planet-circling period of 4.9 days, the feature advances at a rate of 73° day^{-1}, or about 3°.1 hr^{-1}, where "day" and "hour" refer to intervals of 86,400 s and 3600 s, respectively. Based on the time stamps recorded in their data labels, the data cubes `VI0517_03` and `VI0383_00` were obtained precisely 11,560,944 s apart, or 133$^{\rm d}$19$^{\rm h}$22$^{\rm m}$24$^{\rm s}$ apart. That is, the feature had advanced by 9830° longitude since the time that orbit `383_00` was acquired. If we "advect" the feature by 9830° longitude into the past (west to east, against the typical zonal flow), then the feature will have traveled around the planet 27 times, plus an additional 110° longitude. Because the feature was seen at longitude 110° during cube `517_03`, we can deduce that it was in the vicinity of 220° longitude (or −140° (west) longitude) during cube `383_00`. However, our view of Venus at the time of cube `383_00` is limited to the longitude range −60° to 10°. Thus, the feature is reasonably assumed to be located about 100° to the west of our view in Figure 6, meaning that this is a view of the clouds approximately 30 hr in the wake of the passage of the feature. By a similar argument, the view during cube `384_00` is about 170° in the wake, about 54 hr after the passage of the feature, or some 64 hr before its re-appearance.

We hypothesize that the state of the clouds seen during orbits 383 and 384, as seen in Figure 6, possibly shows an example of such a typical post-evolutionary cloud. As was seen in the wake of the feature seen in Akatsuki IR2 data (Peralta et al. 2020), the

extent of the darker cloud region extends to around 30°S latitude (note that the northern hemisphere is out of the field of view for this and most VIRTIS-M-IR mapping mode cubes).

In order to test this hypothesis, we first note that a distinct transition occurs in the orbit 383 and 384 cubes at a latitude of about 35°S—though a bit farther south, and less zonally consistent in the orbit 384 data. We therefore define equatorial and midlatitude regions of interest (ROIs). Because of the time (and/or space) variability in the latitude of this transition region, we conservatively define the equatorial ROI to consist of all points in the observed field of view in the range 0°–30°S and the midlatitude ROI to consist of all points in the field of view that are poleward of 40°S, which in these cubes is approximately 40°S to 65°S. Because none of the cubes analyzed here have significant coverage in polar regions, we do not further apply a southern edge to the south ROI. Because we are examining the possibility that the `VI0383` and `VI0384` cloud in the equatorial ROI is an evolved form of the `VI0517` cloud behind the wall, we further divide the equatorial ROIs of the `VI0517` cubes into ahead and behind ROIs, separated by a 2° longitude boundary, drawn by eye and centered on the observed front. These ROIs are indicated by irregular polygons in Figure 2; because they are defined solely by latitude, we chose not to complicate Figure 6 by adding the ROI to that figure. We then calculate the means and standard deviations of all derived parameters in each of these ROIs and present the summary in Table 1.

Comparing the behind ROIs of orbit 517 with the equatorial ROIs of orbits 383 and 384, we find that most retrieved parameters are consistent, in that the observed interorbit difference is less than (and in some cases much less than) the observed intracube variability in the retrievals of that parameter. However, the retrieved weight percent has decreased significantly by nearly 7% and the size parameter has increased significantly by about 0.1, both of which are consistent with the evolutionary scenario discussed above. Furthermore, while the mean water vapor retrieval is essentially

Table 1
Retrieved Parameters in VIRTIS Regions of Interest

Parameter: ROI	$I_{1.74}$ (W m^{-2} sr^{-1} μm^{-1})	Wt (%)	CO (ppmv)	H$_2$O (ppmv)	z_{base} (km)	m_{size} (unitless)
517_01 Ahead	0.136 ± 0.027	79.6 ± 2.8	26.6 ± 1.2	38.8 ± 1.7	48.4 ± 0.6	0.660 ± 0.022
517_03 Ahead	0.129 ± 0.025	81.1 ± 2.5	25.5 ± 0.9	40.6 ± 2.0	48.7 ± 0.6	0.624 ± 0.022
517_01 Behind	0.0643 ± 0.0105	85.4 ± 2.0	29.0 ± 2.0	28.5 ± 5.1	47.5 ± 0.4	0.638 ± 0.029
517_03 Behind	0.0624 ± 0.0105	85.6 ± 2.0	28.4 ± 3.2	31.2 ± 6.2	47.6 ± 0.5	0.593 ± 0.025
517_01 Mid	0.168 ± 0.043	78.1 ± 3.0	29.2 ± 1.5	37.2 ± 1.9	48.1 ± 0.8	0.697 ± 0.022
517_03 Mid	0.151 ± 0.040	80.6 ± 2.8	27.7 ± 1.5	39.2 ± 2.1	48.3 ± 0.8	0.647 ± 0.025
383_00 Equ	0.0731 ± 0.0149	78.7 ± 2.2	26.0 ± 3.1	26.5 ± 6.2	47.1 ± 0.6	0.712 ± 0.042
383_00 Mid	0.147 ± 0.016	80.9 ± 1.9	29.1 ± 3.0	35.4 ± 2.5	49.8 ± 0.5	0.669 ± 0.024
384_00 Equ	0.0839 ± 0.0193	77.8 ± 2.0	27.7 ± 2.5	26.3 ± 5.6	47.0 ± 0.9	0.733 ± 0.024
384_00 Mid	0.200 ± 0.038	77.5 ± 2.6	30.9 ± 2.9	34.8 ± 2.1	49.7 ± 0.5	0.687 ± 0.030

the same in these ROIs, the intracube variability, as evidenced by the standard deviation, has increased substantially in the notionally more evolved cloud of orbits 383 and 384. This is to be expected because the growth of the cloud particles with time is partially stochastic, responding to smaller-scale variations in the wind speeds that can affect the vertical mixing within the clouds. Hence, this larger inherent variability in the retrieved water vapor mixing ratio is likely the result of a greater variability in the cloud opacity. In fact, we see that the intracube variability in the 1.74 μm radiance is approximately 50%–100% greater in the 383 and 384 orbit observations. All in all, these ROI analyses support the notion of cloud evolution in the aftermath of a Kelvin wave front passage as suggested above. Note, however, that we do not have a positive identification of the feature near in time to this observation by VIRTIS, so this particular conclusion must be considered mere conjecture. Future observations by hyperspectral imagers with long-baseline and high-cadence observational capacity are required to confirm or refute this description of the post-wave front cloud evolution.

5. Conclusions

We present a quasi-spectral analysis, based on previous work by Barstow et al. (2012) and Barstow (2012), of the Giant Dark Cloud feature seen in Akatsuki IR2 imagery, to complement the dynamical analysis of the feature that was presented in Peralta et al. (2020). We find that the feature, though observed to propagate at speeds consistent with the upper part of the middle cloud, has greatest influence on the lower clouds of Venus. This behavior is consistent with the identification by Peralta et al. (2020) of the feature as a front associated with a nonlinear Kelvin wave. That is to say that the nonlinear Kelvin wave drives a density gradient at its crest, which sets into motion a dynamical circulation similar to that seen in the simulations by Baker et al. (1998), in which very strong narrow downwelling plumes are balanced by broader but weaker upwelling regions. We show that the subsequent evolution of the lower and middle clouds in response to the passage of such a feature is consistent with the appearance of the clouds at times when the Giant Dark Cloud is not seen. However, the constraints of the small field of view and observational cadence of VIRTIS on Venus Express limits our ability to confirm this, because the data do not exist to follow the evolution of this feature over days to weeks, as is possible with Akatsuki data. VIRTIS-H, the high spectral resolution near-infrared channel of the VIRTIS instrument, shares a common boresight with

VIRTIS-M-IR, though with a smaller field of view and a narrower spectral range. While, for these reasons, thorough cross-calibration and cross-comparison with the work presented here are not possible, such comparisons where there is simultaneous position and wavelength coverage between VIRTIS-M-IR and VIRTIS-H could lead to significant improvement upon the analyses presented here. Further understanding of the nature of this feature will require both extensive ground-based observations and missions devoted to monitoring planetary atmospheres.

ORCID iDs

Kevin McGouldrick ⓘ https://orcid.org/0000-0003-0328-649X
Javier Peralta ⓘ https://orcid.org/0000-0002-6823-1695
Joanna K. Barstow ⓘ https://orcid.org/0000-0003-3726-5419

References

Allen, D. A., & Crawford, J. W. 1984, Natur, 307, 222
Arney, G., Meadows, V., Crisp, D., et al. 2014, JGRE, 119, 1860
Baker, R. D., Schubert, G., & Jones, P. W. 1998, JAtS, 55, 3
Barstow, J. K. 2012, PhD thesis, Univ. Oxford, https://ora.ox.ac.uk/objects/uuid:b848ae84-264e-4874-ad1e-54a843301287
Barstow, J. K., Tsang, C. C. C., Wilson, C. F., et al. 2012, Icar, 217, 542
Besse, S., Vallat, C., Barthelemy, M., et al. 2018, P&SS, 150, 131
Bézard, B., Tsang, C. C. C., Carlson, R. W., et al. 2009, JGRE, 114, E00B39
Carlson, R. W., Kamp, L. W., Baines, K. H., et al. 1993, P&SS, 41, 477
Cottini, V., Ignatiev, N. I., Piccioni, G., & Drossart, P. 2015, P&SS, 113, 219
Drossart, P., Piccioni, G., Adriani, A., et al. 2007, P&SS, 55, 1653
Emanuel, K. A. 1987, JAtS, 44, 2324
Fedorov, A. V., & Melville, W. K. 2000, JPO, 30, 1692
Fedorova, A., Marcq, E., Luginin, M., et al. 2016, Icar, 275, 143
Gao, P., Zhang, X., Crisp, D., Bardeen, C. G., & Yung, Y. 2014, Icar, 231, 83
Grinspoon, D. H., Pollack, J. B., Sitton, B. R., et al. 1993, P&SS, 50, 515
Ignatiev, N. I., Moroz, V. I., Moshkin, B. E., et al. 1997, P&SS, 45, 427

Imamura, T., & Hashimoto, G. L. 1998, JGR, 103, 31349

Irwin, P. G. J., Teanby, N. A., de Kok, R., et al. 2008, JQSRT, 109, 1136

James, E. P., Toon, O. B., & Schubert, G. 1997, Icar, 129, 147

Knollenberg, R. G., & Hunten, D. H. 1980, JGR, 85, 8038

Marcq, E., Bézard, B., Drossart, P., et al. 2008, JGRE, 113, E00B07

McGouldrick, K. 2017, EP&S, 69, 161

McGouldrick, K., Momary, T. W., Baines, K. H., & Grinspoon, D. H. 2012, Icar, 217, 615

McGouldrick, K., & Toon, O. B. 2007, Icar, 191, 1

McGouldrick, K., & Toon, O. B. 2008, P&SS, 46, 1112

Moinelo, A. C., Piccioni, G., Ammannito, E., Filacchione, G., & Drossart, P. 2010, ITGRS, 48, 3941

Nakamura, M., Imamura, T., Ueno, M., et al. 2007, P&SS, 55, 1831

Peralta, J., Navarro, T., Vun, C. W., et al. 2020, GeoRL, 47, e87221

Piccioni, G., Drossart, P., Suetta, E., et al. 2008, ESA SP-1295, VIRTIS: The Visible and Infrared Thermal Imaging Spectrometer (Noordwijk: ESA)

Pollack, J. B., Dalton, J. B., Grinspoon, D. H., et al. 1993, Icar, 103, 1

Pollack, J. B., Toon, O. B., & Boese, R. 1980, JGR, 85, 8223

Satoh, T., Sato, T. M., Nakamura, M., et al. 2017, EP&S, 69, 154

Satoh, T., Vun, C. W., Sato, T. M., et al. 2019, EPSC, 13, 1558

Steele, H. M., & Hamill, P. 1981, JAerS, 12, 517

Svedhem, H., Titov, D., Taylor, F., & Witasse, O. 2009, JGRE, 114, E00B33

Tsang, C. C. C., Irwin, P. G. J., Taylor, F. W., & Wilson, C. F. 2008, JQSRT, 109, 1118

Wilson, C. F., Guerlet, S., Irwin, P., et al. 2008, JGRE, 113, E00B13

Yung, Y. L., Liang, M. C., Jiang, X., et al. 2009, JGRE, 114, E00B34